A SEARCH FOR FAST RADIO BURSTS ASSOCIATED WITH GAMMA-RAY BURSTS

Divya Palaniswamy[1], Randall B. Wayth[1], Cathryn M. Trott[1,2], Jamie N. McCallum[3],
Steven J. Tingay[1], and Cormac Reynolds[1]
[1] International Centre for Radio Astronomy Research, Curtin University, Bentley, WA 6102, USA; divya.palaniswamy@postgrad.curtin.edu.au
[2] ARC Centre of Excellence for All-Sky Astrophysics (CAASTRO), 44 Rosehill Street Redfern, NSW 2016, Australia
[3] University of Tasmania, Hobart, Tasmania, 7001, Australia

ABSTRACT

The detection of seven fast radio bursts (FRBs) has recently been reported. FRBs are short duration (∼1 ms), highly dispersed radio pulses from astronomical sources. The physical interpretation for the FRBs remains unclear but is thought to involve highly compact objects at cosmological distance. It has been suggested that a fraction of FRBs could be physically associated with gamma-ray bursts (GRBs). Recent radio observations of GRBs have reported the detection of two highly dispersed short duration radio pulses using a 12 m radio telescope at 1.4 GHz. Motivated by this result, we have performed a systematic and sensitive search for FRBs associated with GRBs. We have observed five GRBs at 2.3 GHz using a 26 m radio telescope located at the Mount Pleasant Radio Observatory, Hobart. The radio telescope was automated to rapidly respond to Gamma-ray Coordination Network notifications from the *Swift* satellite and slew to the GRB position within ∼140 s. The data were searched for pulses up to 5000 pc cm^{-3} in dispersion measure and pulse widths ranging from 640 μs to 25.60 ms. We did not detect any events ⩾6σ. An in depth statistical analysis of our data shows that events detected above 5σ are consistent with thermal noise fluctuations only. A joint analysis of our data with previous experiments shows that previously claimed detections of FRBs from GRBs are unlikely to be astrophysical. Our results are in line with the lack of consistency noted between the recently presented FRB event rates and GRB event rates.

Key words: gamma-ray burst: general – methods: statistical

Online-only material: color figures

1. INTRODUCTION

Gamma-ray bursts (GRBs) are among the most powerful objects in the universe. The energy output in the γ-rays is in the order of 10^{51} erg (assuming isotropic emission) on second timescales at cosmological distances (Rees & Meszaros 1994; Ghirlanda et al. 2006). GRBs are divided into two classes, short and long, which are usually defined by T_{90} (Kouveliotou et al. 1993), the time during which the cumulative counts in the detector increases from 5% to 95% above the background rate. There are two types of plausible central engine model proposed for GRBs: (1) stellar mass black holes, which accrete material from a remnant star with an extremely high accretion rate (∼(0.1–1) $M_\odot$ s^{-1}; Popham et al. 1999; Narayan et al. 2001; Lei et al. 2013); and (2) rapidly rotating (∼ms duration), highly magnetized neutron stars (a proto-magnetar; Usov 1992; Rowlinson et al. 2010; Fan et al. 2013a). Based on the latter model of the central engine, Usov & Katz (2000) proposed that GRBs may be accompanied by very bright, short duration (⩽ms) radio bursts, which could be observed at frequencies of tens of MHz. Detection of such radio emission from a GRB at a cosmological distance could provide a probe for understanding both the ionized intergalactic medium (IGM) and GRB physics (Palmer 1993; Ioka 2003; Ghirlanda et al. 2006). However, Macquart (2007) showed that observations of short duration radio pulses from GRBs at low radio frequencies (∼10–100 MHz) would be significantly limited by scattering effects because the radio emission passes through the dense stellar wind of the progenitor or the immediate interstellar medium surrounding the source. Macquart (2007) showed that these propagation effects alter the properties of radiation with brightness temperature ≫10^{10} K, which may hinder the detectability of any radio pulse.

Recently, Zhang (2014) proposed that GRBs (with a magnetar as the central engine) could produce short duration radio pulses when the supra-massive neutron stars undergo rapid spin down (due to strong magnetic fields) within 10^2–10^3 s of their birth, collapsing into black holes as they lose centrifugal support. These short duration radio pulses are proposed to be detectable at radio frequencies ranging from 1.2 to 1.5 GHz, if they are not absorbed by the GRB blast wave in front of the emission region. Zhang (2014) suggests that a small fraction of short duration radio pulses could be physically connected with GRBs.

In recent years, there have been number of detections of non-repeating short duration radio pulses. The dispersion measures (DMs) of these pulses are so large that the progenitors are suggested to be extragalactic in origin. Lorimer et al. (2007) reported the discovery of the first such short duration radio pulse; they discovered a single pulse of duration ∼5 ms at a DM of 375 pc cm^{-3} from archival data (Manchester et al. 2006) recorded using the 64 m Parkes radio telescope. Lorimer et al. (2007) inferred an event rate of 50 day^{-1} Gpc^{-3} (assuming an isotropic distribution of the sources in the sky) and proposed that the implied rates of occurrence were compatible with GRB rates. However, there are no recorded GRB events[4] near the pulse location. Another event was discovered by Keane et al. (2011) from archival data (Manchester et al. 2001) with the same telescope. The pulse properties were similar to that reported by Lorimer et al. (2007), with a short timescale (∼7 ms) and high DM (745 pc cm^{-3}). Recent analysis of this pulse has suggested it is Galactic in origin (Bannister & Madsen 2014).

Some doubts on the extragalactic origin of these pulses have been put forward, based on the work of Burke-Spolaor et al.

---

[4] In this case, a GRB event could have been simply missed, since no γ-*ray* satellite was observing at the time and position of the event.

(2011), with the detection of 16 similar highly dispersed pulses from Parkes archive data (Edwards et al. 2001; Roberts et al. 2002; Crawford et al. 2006; Jacoby et al. 2009), all deemed as being terrestrial in origin. Most recently, however, the evidence for an extragalactic origin has strengthened significantly with the discovery of four new highly dispersed pulses by Thornton et al. (2013). Thornton et al. (2013) coined the term fast radio burst (FRB) to describe these bursts. The FRBs were detected with DMs in the range 553–1103 pc cm^{-3}. Based on their properties, Thornton et al. (2013) infer the FRB event rate ($R_{\rm FRB}$) to be 10^{-3} yr^{-1} galaxy^{-1} in the comoving sample volume that contains $\sim 10^9$ late type galaxies, which is $\sim 10^3$ times larger than the GRB rates ($R_{\rm GRB} = 10^{-6}$ yr^{-1} galaxy^{-1}). Using the inconsistency in the event rates and, in particular, with no known GRB events coincident with the FRBs, Thornton et al. (2013) rule out GRBs as possible progenitors for most FRBs.

All six FRBs mentioned above were detected by the 64 m Parkes radio telescope and its 13 beam receiver, creating concerns about the astrophysical origin of the pulses. Most recently, Spitler et al. (2014) reported a discovery of a seventh FRB in the 1.4 GHz Pulsar ALFA survey with the 300 m Arecibo telescope, the first FRB discovered from a geographical location other than Parkes. This FRB was found at low galactic latitude ($b = -0°.2$) with a DM of 557.4 pc cm^{-3} and pulse width ~ 3 ms. Despite the low galactic latitude, the high DM suggests an extragalactic origin.

None of the FRBs from Parkes or Arecibo to-date have been associated with a GRB, although the theoretical possibility that they might be connected has motivated several experiments to look for coincident GRB/FRB emission. Bannister et al. (2012, hereafter B12) performed a targeted survey to detect short duration radio pulses from GRBs at 1.4 GHz. B12 observed nine GRBs, both long and short, using a 12 m radio telescope located at the Parkes Observatory. B12 reported the detection of two single radio pulses from two long GRBs with signal to noise ratio (S/N) > 6σ. The pulses were detected 524 and 1076 s after the γ-ray emission from the GRBs. The DMs of the pulses were 195 pc cm^{-3} and 570 pc cm^{-3}, which are large compared to the expected Galactic electron-density contribution (Cordes & Lazio 2002) to the DM, indicating the possibility that the bursts are extragalactic in origin and possibly from the GRBs.

Similar to the B12 experiment, there have been a number of past and ongoing experiments searching for FRB-like emission from the prompt phase of GRBs at low and high radio frequencies (Obenberger et al. 2014; Staley et al. 2013; Balsano 1999; Benz & Paesold 1998; Baird et al. 1975). Baird et al. (1975) observed 19 GRB events at 151 MHz between 1970 and 1973, with a time resolution of 0.3 s; they searched for coincident radio pulses with two or more stations over periods -1 hr to $+10$ hr relative to the GRB event times. Their search failed to locate any astronomical radio pulse above their sensitivity limit of 10^5 Jy. Two other GRBs were observed by Dessenne et al. (1996), who performed an automatic rapid radio follow-up experiment at 151 MHz, with a time resolution of 1.5 s; they reported a non-detection at a sensitivity of 3σ of 73 Jy. Benz & Paesold (1998) observed 7 GRBs between 1992 and 1994, covering a large range of frequencies between 40 and 1000 MHz using three similar spectrometers, with a time resolution of 0.15 s. Although the experiment sensitivity was low (10^5 Jy), the spectral coverage made this experiment very interesting. Similarly, Balsano (1999) observed 32 GRBs at 73.75 MHz from 1997 to 1998 and had a wide range of sensitivity for each GRB.

They reported a non detection at sensitivity limit of ~ 200 Jy for integration times of 50 ms.

Most Recently, Obenberger et al. (2014) reported the observations of 12 GRBs at 74 MHz, five GRBs at 52 MHz, and 17 GRBs at 37.9 MHz with a time resolution of 5 s. Similarly, Staley et al. (2013) reported the observation of four GRBs at 15 GHz with a time resolution of 0.5 s. Both Staley et al. (2013) and Obenberger et al. (2014) did not detect any FRB-like emission from the observed GRBs.

The sensitivities of the above mentioned experiments were generally low, however they have motivated a number of follow-up experiments including this work and a recent follow up project (VLBA project codes BB317 and BB325)[5] to use one or more Very Long Baseline Array (VLBA; Napier et al. 1994) dishes to automatically follow up GRB alerts during telescope idle time. The VLBA-GRB experiment searches for FRBs using the existing V-FASTR system (Wayth et al. 2011).

In this paper, we describe observations performed at 2.3 GHz using the Hobart 26 m radio telescope to search for FRBs associated with GRBs. We designed our experiment to be similar to the B12 experiment with some improvements. Our aim was to observationally test the possible association of FRBs with GRBs and compare our results with the B12 results. Section 2 of this paper describes the observations performed. A detailed description of our single pulse search pipeline and verification is given in Section 3. In Section 4, we analyze our results and compare them with the B12 results. Conclusions are presented in Section 5.

2. OBSERVATIONS

We observed the five GRBs listed in Table 1 at a central frequency of 2.276 GHz using the 26 m radio telescope located at the Mount Pleasant Radio Observatory operated by the University of Tasmania[6] near Hobart, Tasmania. A computer at the observatory is configured to receive GRB notifications via email from the Gamma-ray Coordination Network (GCN).[7] The GCN system distributes the location of the GRBs detected by space-borne observatories such as *Integral* (Winkler et al. 2003), *Swift* (Gehrels et al. 2004), *Agile* (Tavani et al. 2009), and *Fermi* (Atwood et al. 2009) in real time. A filter is applied to accept notices only from the *Swift* satellite, hence the GRBs listed in Table 1 are all observed by the *Swift* satellite. The gamma-ray Burst Alert Telescope (BAT) on *Swift* first detects the GRB and localizes the burst direction to an accuracy of $\sim 3'$. These are the co-ordinates used by the telescope control system. Given that the radio telescope's primary beam full width at half maximum for this experiment is about 0°.35, all the observed GRBs in this experiment fall within the beam. Only GRBs that are above the elevation limit (12°) and within the visible range of the telescope ($-90° < \delta < +30°$) are observed. When an accessible GRB is identified, the telescope slews to the listed coordinates and then starts recording data. On average, it takes approximately 140 s for the telescope to slew to the required location.

Data were recorded using the Australian Long Baseline Array (LBA) Data Acquisition System (DAS[8]; Phillips et al. 2009). The LBA DAS has a sampler and digital filter which receives two independent analog intermediate frequencies (IFs), the right

Table 1
Details of Five GRBs Observed using the 26 m Radio Telescope

Source	α (J2000.0)	δ (J2000.0)	P_{BAT} (arcmin)	Trigger Date	T_{BAT} (UT)	T_{alert} (UT)	T_{90} (s)	T_{rec} (UT)	T_{obs} (s)	T_{XRT} (UT + s)
GRB 111212A	$+20^h41^m37^s$	$-68°37'01''$	3	2011 Dec 12	09:23:07	09:24:06	30.86	09:24:50	1200	$T_{BAT} + 2856$
GRB 120211A	$+05^h51^m00^s$	$-24°45'32''$	3	2012 Feb 11	11:58:28	11:59:29	101	12:03:10	1800	$T_{BAT} + 119.5$
GRB 120212A	$+02^h52^m25^s$	$-18°01'29''$	3	2012 Feb 11	09:11:22.74	09:11:43	20.42	09:13:20	1800	$T_{BAT} + 2676$
GRB 120218A[a]	$+21^h19^m02^s$	$-25°27'00''$	3	2012 Feb 18	00:49:22.14	00:50:17	7	00:52:10	1800	. . .
GRB 120224A	$+02^h43^m54^s$	$-17°47'32''$	2.4	2012 Feb 24	04:39:56.49	04:40:40	2.06	04:42:00	1800	$T_{BAT} + 109.1$

Notes. P_{BAT} is the BAT position uncertainty, T_{BAT} is the time when BAT detected a GRB, T_{alert} is the time when the GCN alert notifications were sent, T_{90} is the GRB duration based on the BAT light curve, T_{rec} is the time when the recorders at 26 m Hobart telescope started recording the data from the source, T_{obs} is the observation duration with the radio telescope and T_{XRT} is the time when X-ray data were recorded by the XRT on *Swift*.
[a] No XRT light curve due to Sun observing constraints. *Swift* could not slew to the BAT position until 19:14 UT on 2012 Feb 20.

and left circular polarized signals over a 64 MHz bandwidth. The analog IFs are sampled and digitized to 8 bit precision and then re-sampled to 2 bits using digital filters (Phillips et al. 2009) before the digital representation of the voltage is recorded to computer disk. For each observation the system equivalent flux density (SEFD) of the telescope was measured to be 800–900 Jy, which is calculated as SEFD = $(8\, k_B\, T_{sys}/\eta_a\, \pi\, D^2)$ where T_{sys} is the system temperature (92–103 K), k_B is the Boltzmann constant, η_a and D are the antenna efficiency (0.6) and the diameter of a circular aperture antenna (26 m), respectively. The automatic gain control loops were turned off for the duration of the observations. The 1σ flux density sensitivity for the 26 m telescope (to detect a pulse of width 25 ms) is approximately 0.5 Jy, calculated as $\sigma = (\text{SEFD}/\sqrt{\triangle f\, \triangle t\, n_p})$ where $\triangle f$ and $\triangle t$ are the bandwidth (64 MHz) and integration time (25 ms), respectively, and n_p is the number of polarizations (2). The pointing error of the 26 m telescope across the whole sky is ~21''.

The observations occurred over a period of 30 minutes for each GRB except for GRB 111212A which was observed for 20 minutes. Following observation of the GRB field, the telescope slewed to a nearby calibrator[9] and data were recorded for 20 minutes. A control observation was then undertaken by pointing the telescope at blank sky (~2° away from the GRB position) for approximately 20 minutes and recording the voltage data.

3. PROCESSING AND VERIFICATION

The recorded data were transferred to the petabyte data storage facility at iVEC,[10] in Perth. Data processing was performed on the Curtin University Parallel Processor for Astronomy (CUPPA), a 20 node computer cluster operated by Curtin University.

3.1. Single Pulse Search Pipeline

In this section, we describe the data processing pipeline (Figure 1) used to search for single short duration radio pulses in our data. The search pipeline has multiple stages: correlation; time averaging; radio frequency interference (RFI) excision; dedispersion; event detection; and classification of events. Several of our tools were reused from the V-FASTR experiment (Wayth et al. 2011), which can read LBA data natively.

3.1.1. Correlation

The first step in the processing pipeline was to pass the data through a spectrometer to form channelized total power for each polarization. The 2 bit digitized voltage samples from each polarization were decoded and sent to a software correlator. The correlator is an FX[11] design with a configurable number of spectral channels and averaging time. We used 128×0.5 MHz spectral channels, formed via FFT, and an averaging time of $640\,\mu$s. The output of the software correlator was written to files for subsequent processing.

3.1.2. Time Averaging

The intrinsic width of pulses are generally unknown. Because the dispersion and scattering affects the observed width of the pulse, a large parameter space of pulse widths must be searched (Cordes & McLaughlin 2003). To obtain optimal sensitivity, the correlated time series were averaged for pulse widths ranging from 1.28 ms to 20.48 ms. This was achieved by averaging 2^n time samples together, where n ranges from 1 to 5, and searching each averaged time series independently. An additional time averaged series was generated at 25.60 ms by averaging 40 time samples together (which is not a power of two), to match the width used by B12 in their experiment.

3.1.3. RFI Excision

Observations at 2.3 GHz are generally affected by RFI from terrestrial transmitters, radars, satellites etc., which changes the total power as a function of frequency and time. Therefore, identification and excision of RFI was undertaken.

First, we excise the time samples in each frequency channel that were affected by sporadic RFI. The top panel of Figure 2 shows an example of sporadic, wide-band RFI, where the power level in all the frequency channels over short timescales (in this case ~4 ms) is much higher when compared to the typical mean power in neighboring time samples across the frequency band. The top panel of Figure 3 shows an example of sporadic narrow-band RFI, where the power level in a frequency channel over a short time (in this case ~640 μs) is high when compared to the typical mean power in the neighboring time samples in that frequency channel. Our RFI excision algorithm used a thresholding method to identify samples in the time domain which were affected by RFI. First, we calculated the local variance (σ_l^2) of the time samples in each frequency channel over an adjustable time range (~10 s) and then compared to the power (amplitude) of each time sample. The time samples

---

[9] LBA calibrators list—www.atnf.csiro.au/vlbi/observing/fringefinders.html
[10] www.ivec.org/about/

[11] F is the Fourier transform and X is the cross multiplication.
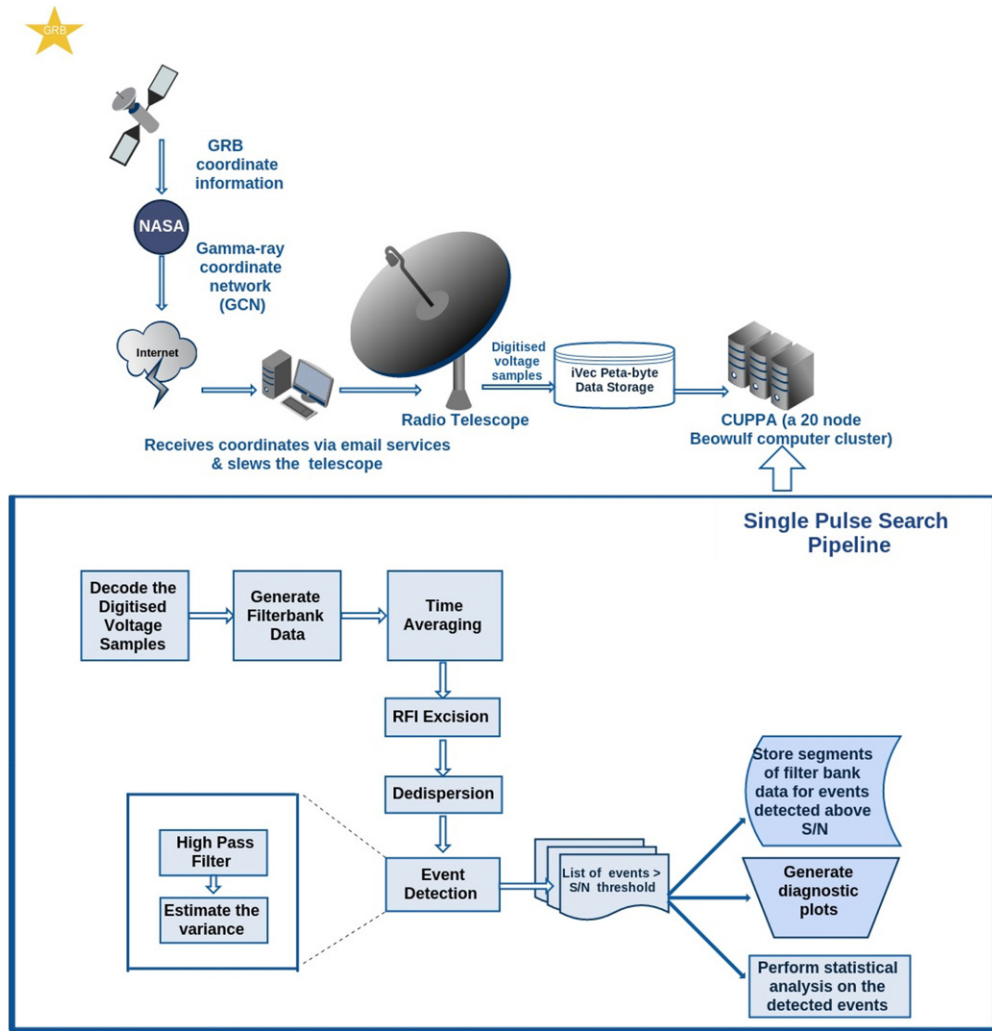
Figure 1. Top panel: a schematic representation of the system where the space-borne GRB telescope sends the position information for GRBs to our ground-based radio telescope through GCNs. The radio telescope is then slewed to the GRB positions and data are recorded. The recorded data are then transferred to the petabyte data storage facility at iVEC in Perth and processed on a 20 node Beowulf computer cluster, CUPPA. Bottom panel: the single pulse search pipeline implemented in this paper to search for FRBs from GRBs. The search pipeline has multiple stages: correlation; time averaging; radio frequency interference (RFI) excision; dedispersion; event detection; and classification. In this experiment we generate time averages ranging from 640 μs to 25.60 ms (Section 3.1.2). Each averaged time series goes through the RFI excision, dedispersion, event detection, and classification stages independently.

(A color version of this figure is available in the online journal.)

that exceeded a pre-set threshold (here the threshold was set to $5\sigma_l$) were excised from the time series and replaced with the mean power value estimated for each frequency channel over the band. We conservatively chose a $5\sigma_l$ threshold for RFI excision, because we did not want to clip the thermal noise distribution.[12] The bottom panels of Figures 2 and 3 show the results of our excision algorithm.

Next, we manually identified and excised persistent narrow-band RFI which are constant in time over a frequency channel. The top panel of Figure 2 shows an example of persistent narrow-band RFI where the power in a frequency channel is higher compared to the power in the neighboring channels across the

frequency band. The affected channels, including the lower band edge spectral channel (DC channel generally has spurious high power due to sampler offsets), were recorded in a flagging file. The dedisperser (the next stage in the pipeline) reads the flagging files for bad channels and ignored the bad channels in further processing. We repeated the RFI excision process on all the time averaged data series.

3.1.4. Dedispersion

The next step in the pipeline is dedispersion. Any incoming astronomical impulsive radio signal will, in general, be dispersed in time across the spectral channels due to the ionized component of the interstellar and IGMs (Lorimer & Kramer 2012). The intrinsic signal can largely be recovered by incoherent dedispersion, by applying an appropriate time delay for each spectral channel and adding power across all the spectral channels. The time delay between two frequencies is given by $\Delta t = 4.15\,\text{ms} \times \text{DM} \times (\nu_{lo}^{-2} - \nu_{hi}^{-2})$, where the DM (pc cm^{-3}) is the integrated column density of free electrons along the line of sight and ν_{lo} and ν_{hi} are the low and high frequencies in GHz, respectively (Lorimer & Kramer 2012).

---

[12] Assuming the power level in the data follows the normal distribution, the probability of detecting an event above some significant threshold due to thermal noise fluctuations in the data is determined using the cumulative distribution function (see Section 4.2). Thus the probability of detecting an event $>5\sigma$ is 2.87×10^{-7} and for $>3\sigma$ the probability is 1.3×10^{-3}. We have $\sim 2 \times 10^6$ independent samples, therefore, at 5σ we would be effectively clipping $\sim$one sample as a false positive, compared to when a 3σ threshold is chosen we would be effectively clipping $\sim$2600 samples. This could skew the thermal noise distribution in the data.
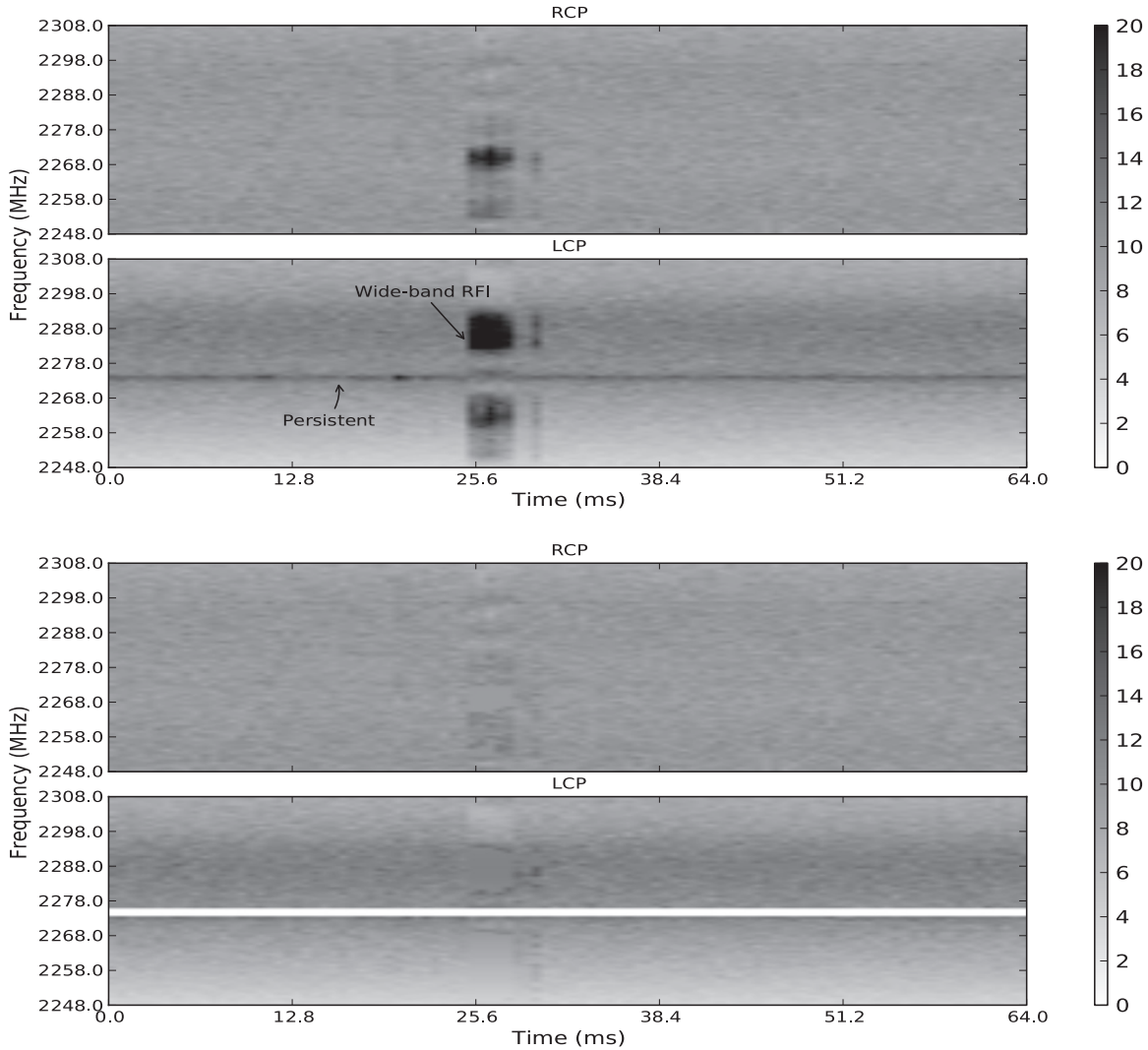
Figure 2. Example dynamic spectrum shows RFI excision. Intensity is arbitrary power units. Top panel: an example of a wide-band RFI and persistent narrow-band RFI. Bottom panel: the results of RFI excision algorithm on the data.

Table 2
For Each Time Average, the Table Lists the Number
of DM Steps used to Dedisperse the Data

Time Averaging (ms)	N_{DM}
0.64	149
1.28	114
2.56	79
5.12	45
10.24	23
20.48	12
25.60	9

We use Dedisperser of Autocorrelations for Radio Transients (DARTs) to perform the incoherent dedispersion, a detailed description of which is given by Wayth et al. (2011). The incoming data to DART are ordered in frequency and time for each polarization. The dedispersion process sums the power across channels, with the delay for each channel according to the frequency and DM. At the output, DART combines both polarizations and generates a dedispersed time series for each DM. We dedisperse the data with DM steps as listed in Table 2 ranging from 0 to 5000 pc cm^{-3}. The choice of DM steps was

made by setting the time delay (Δt) between the highest (ν_{hi}) and lowest (ν_{lo}) spectral channels equal to the data sampling time (integration time). Choosing DM steps smaller than the data sampling time leads to highly correlated time samples, since the dedispersed time series are virtually identical for neighboring DM steps. DART is flexible when compared to the Taylor tree algorithm (Taylor 1974) because it can dedisperse the signals beyond the diagonal DM, the DM where the gradient of the dispersion curve is one time sample per spectral channel. The DM steps across the DM range are linearly distributed for the first few DM steps before progressing geometrically, with a growth rate of 1.02. This results in equal spacings at lower DM and increasingly larger spacings at higher DM. Table 2 summarizes the number of DM steps used for each time average.

3.1.5. Event Detection

The next step in the pipeline is detection. After dedispersion, each time series is searched for events above a defined signal to noise threshold. In the detector, the time series are divided into small time segments ($\sim$1.3 s). We chose this length of time because visual inspection of the data showed that the total power sometimes changed on timescales longer than this. If longer time segments were used, this would artificially raise the variance
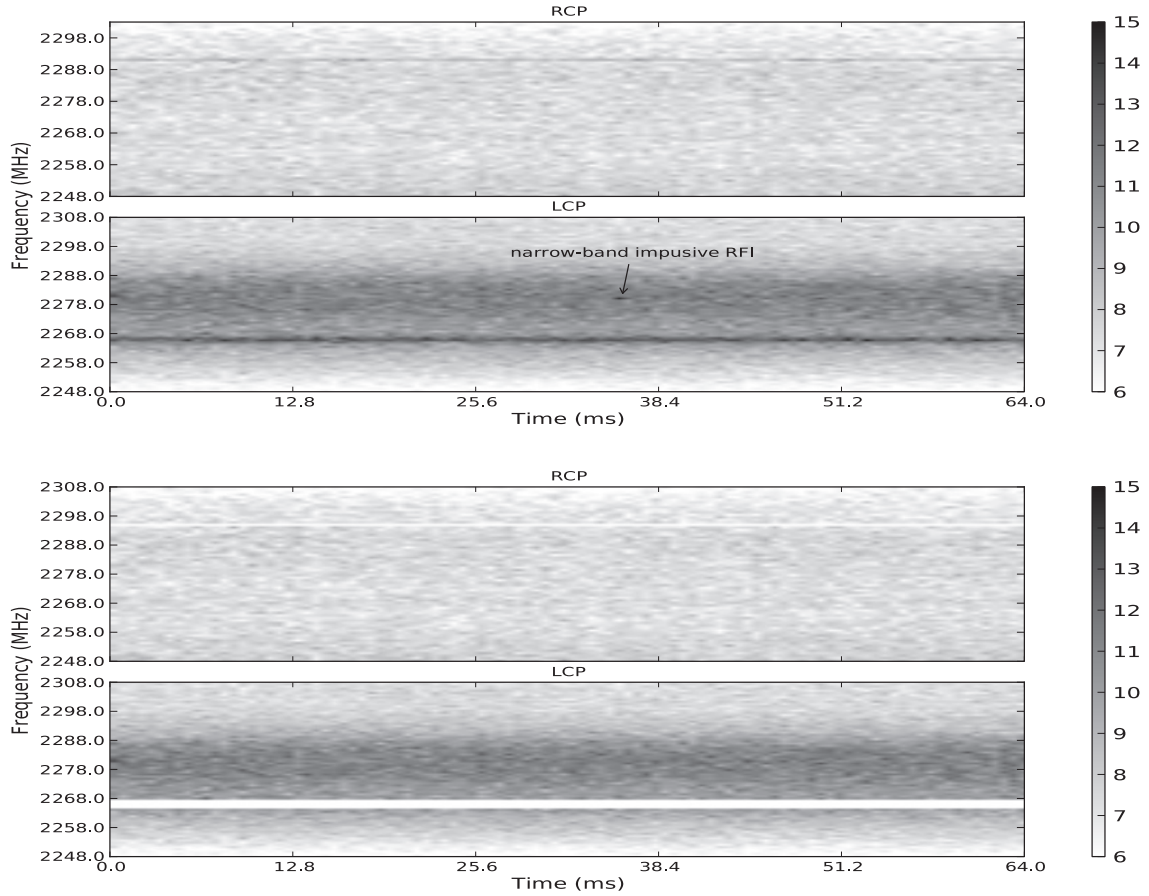
Figure 3. Example dynamic spectrum shows RFI excision. Intensity is arbitrary power units. Top panel: an example of a narrow-band impulsive RFI. Bottom panel: the results of RFI excision algorithm on the data.

estimate. Each time segment is high-pass filtered, by subtracting a 100 time step moving average from each sample. This reduces any long term power variations due to system temperature (T_{sys}) changes, atmosphere, receiver response, etc., that may bias variance estimates on timescales of 100 s of samples while retaining sensitivity to short timescale variations. We note that the high-pass filter window is longer than the expected pulse width of an astronomical event.

Each dedispersed time segment is then searched for single events $>5\sigma$. The noise level of the time series for each DM step is estimated using the standard deviation. We also tried the robust trimmed estimator, interquartile range (IQR; Fridman 2008), to estimate the noise level for each DM step. The number of events detected $>5\sigma$ from the IQR and standard deviation techniques did not differ. We adopt use the standard deviation because the behavior of this statistic is well understood when a finite number of samples are used for its estimation.

3.1.6. Classification of Detected Events $>5\sigma$

The next step in the pipeline is the classification of detected events $>5\sigma$. Figure 4 demonstrates the differences between the signatures of astronomical signals, low level RFI and thermal noise fluctuations in the DM/time plane. An astronomical signal is expected to show reduced S/N for DM steps away from the true DM. The astronomical signals are broad band and any signals well above the minimum detection threshold are expected to be seen in multiple DM steps for a given time average and also in the consecutive time averages. Events due to thermal noise fluctuations will be seen at a single DM step and follow Gaussian statistics (most of the events would be close
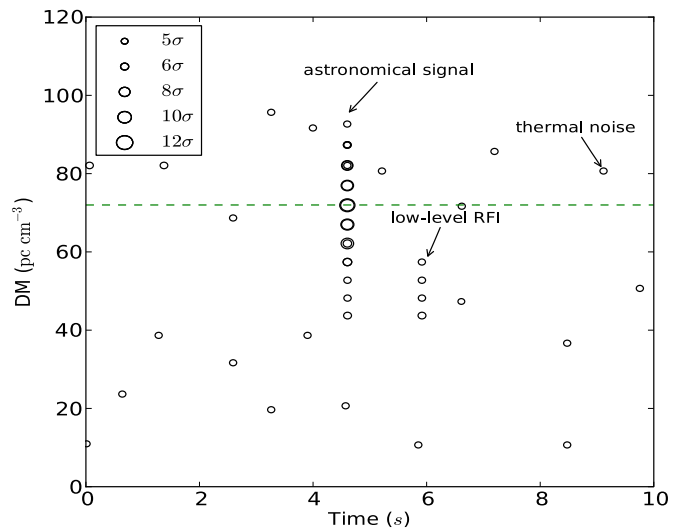
Figure 4. Example diagnostic plot that demonstrates the difference between the signatures of astronomical signals, low level RFI and thermal noise fluctuations in the DM/time plane. The astronomical signal shows reduced S/N for DM steps away from the true DM (dashed line). The events due to thermal noise fluctuations appear at a single DM step. The events due to low level RFI are detected across multiple DM steps, but do not have the characteristic peaked shape that a bright pulse from an astronomical source would have. The size of the circles is proportional to the S/N.

to the S/N threshold). Events due to low level RFI will appear in multiple DM steps, but do not have the characteristic peaked shape that a bright pulse from an astronomical source would have.
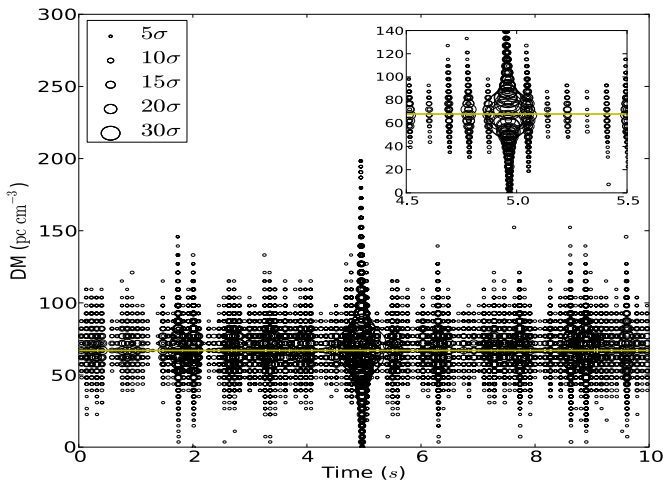
Figure 5. Vela pulsar events detected $>5\sigma$ vs. DM (pc cm^{-3}) as a function of time. The size of the circles are proportional to the signal to noise ratio. Single pulses from Vela are detected at the true DM (horizontal line) and across multiple DM steps with reduced S/N.

(A color version of this figure is available in the online journal.)

3.2. Single Pulse Search Pipeline Verification

To test our single pulse search pipeline we used archival observations of the pulsar PSR J0835−4510 (the Vela pulsar). Observations were made using the same 26 m radio telescope as used for our GRB observations. The data recording system used was also identical to the recorder used for the GRB observations. Vela was observed at a central frequency of 1440 MHz with right and left circular polarizations over a 64 MHz bandwidth. Vela has a steep spectral index, $\alpha = -1.2$ ($S \propto \nu^{\alpha}$), DM = 67.99 pc cm^{-3} and a period of 89.3 ms (Manchester et al. 2005).

The recorded voltage data were correlated at 640 μs time resolution and 128 spectral channels, the same as for the GRB data. The correlated data were dedispersed over a DM range of 0–200 (pc cm^{-3}), with 40 DM steps. The dedispersor output was searched for pulses above the S/N threshold of 5 at 640 μs time averaging and resulting events were examined to determine if they were real pulses from the pulsar in the time/DM plane (Figure 5). Individual pulses were detected at DM $\sim$ 67 pc cm^{-3} and at neighboring DM steps with reduced S/N as expected. Segments of data were written out for each candidate pulse for further investigation. In the follow-up process, candidates were visually inspected via dynamic spectrum plots similar to those shown in Figure 6. The dynamic spectrum shows individual dispersed pulses with a period of 89.3 ms in time across the frequency band. Therefore, we have confirmed detection of individual pulses with Vela's period and DM via our single pulse search pipeline.

4. RESULTS AND DISCUSSION

4.1. Results

Here we discuss the results of our search for FRBs associated with GRBs using the single pulse search pipeline. The five GRBs have $T_{90} > 2$ s based on the light curves from BAT. Processing the five data sets and visually inspecting the events via diagnostic
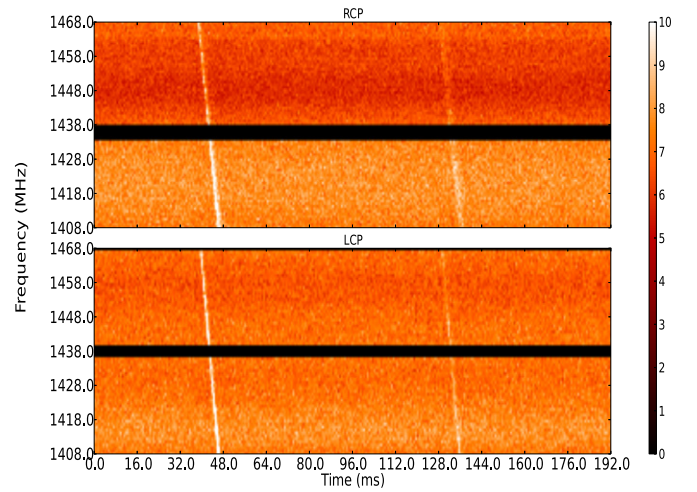
Figure 6. Dynamic spectrum for Vela pulsar, time vs. frequency. The colorbar represents the channel power in arbitrary units. A strong pulse is seen at the left of the plot, followed by a relatively weak pulse, separated by $\sim$89.3 ms, which is the correct period for Vela.

(A color version of this figure is available in the online journal.)

plots did not show any signatures of astronomical signals. All the events detected by our detector were between 5σ and 6σ and no events $\geqslant 6\sigma$ were detected. Table 3 lists the number of $>5\sigma$ events for all the GRBs and time averages, respectively. Figure 7 shows an example diagnostic plot that illustrates the distribution of detected events $>5\sigma$ for GRB 120211A at 1.28 ms time average.

In the absence of a characteristic signature of an astronomical signal $>6\sigma$, we performed a statistical analysis on events between 5 and 6σ to check if they were consistent with expectations due to thermal noise fluctuations. This analysis gives us confidence that our search pipeline is working correctly and highlights the importance of sample variance in determining the significance of an event.

4.2. Statistical Analysis of the Detected Events $>5\sigma$

Here we compare the number of events expected due to thermal noise fluctuations to the number of events recorded by our pipeline. The number of events expected due to thermal noise fluctuations, $N_E(I)$, above the detection threshold is given by

$$N_E(I > 5\sigma) = N_t \, N_{DM} \, P(I > 5\sigma), \quad (1)$$

where N_{DM} is the number of independent DMs, N_t is the number of independent time samples, and $P(I > 5\sigma)$ is the probability of an event above 5σ due to thermal noise fluctuations (assuming the power fluctuation due to thermal noise follows the Gaussian distribution), and is given by the cumulative distribution function (CDF),

$$P(I > 5\sigma) = \int_{5\sigma}^{\infty} \mathcal{N}(\mu, \sigma^2) = \frac{1}{2} + \frac{1}{2}\mathrm{erf}\left[\frac{\mu - 5\sigma}{\sqrt{2}\sigma}\right], \quad (2)$$

where erf is the error function and $\mathcal{N}(\mu, \sigma^2)$ is the Gaussian distribution with mean μ and variance σ^2.

4.2.1. Independent DM Steps

In Equation (1), we note that the N_{DM} steps should be independent. Given our choice of step progression, we expect $\sim$50% of power samples to be identical between consecutive

Table 3
A Summary of the Statistical Analysis Performed on all the GRB Data Sets

| GRB Name	$N_E(I > 5\sigma)$	$N_A(I > 5\sigma)$	$\sqrt{N_E(I > 5\sigma)}$	Δ_N	δE	p
(a) 640 μs						
GRB 111212A[a]	83	85	9	49	49	0.48
GRB 120211A	125	120	11	70	70	0.53
GRB 120212A	125	125	11	70	70	0.50
GRB 120218A	125	129	11	70	70	0.48
GRB 120224A	125	128	11	70	70	0.48
(b) 1.28 ms						
GRB 111212A[a]	32	26	6	36	36	0.56
GRB 120211A	48	42	7	54	54	0.54
GRB 120212A	48	48	7	54	54	0.50
GRB 120218A	48	40	7	54	54	0.55
GRB 120224A	48	51	7	54	54	0.48
(c) 2.56 ms						
GRB 111212A[a]	11	12	3	18	18	0.48
GRB 120211A	16	12	4	26	26	0.56
GRB 120212A	16	22	4	26	26	0.41
GRB 120218A	16	18	4	26	26	0.47
GRB 120224A	16	22	4	26	26	0.56
(d) 5.12 ms						
GRB 111212A[a]	3	1	...	...	...	0.72
GRB 120211A	4	3	...	...	...	0.80
GRB 120212A	4	3	...	...	...	0.80
GRB 120218A	4	1	...	...	...	0.99
GRB 120224A	4	4	...	...	...	0.54
(e) 10.24 ms						
GRB 111212A[a]	0	1	...	...	...	0.21
GRB 120211A	0	1	...	...	...	0.30
GRB 120212A	0	0	...	...	...	1.00
GRB 120218A	0	0	...	...	...	1.00
GRB 120224A	0	0	...	...	...	1.00
(e) 20.48 ms						
GRB 111212A[a]	0	0	...	...	...	1.00
GRB 120211A	0	0	...	...	...	1.00
GRB 120212A	0	0	...	...	...	1.00
GRB 120218A	0	0	...	...	...	1.00
GRB 120224A	0	0	...	...	...	1.00
(e) 25.6 ms						
GRB 111212A[a]	0	0	...	...	...	1.00
GRB 120211A	0	0	...	...	...	1.00
GRB 120212A	0	0	...	...	...	1.00
GRB 120218A	0	0	...	...	...	1.00
GRB 120224A	0	0	...	...	...	1.00

Notes. The subtables (a), (b), (c), (d), and (e) list the time averages used in this experiment. The columns are: the source name, $N_E(I > 5\sigma)$ is the expected number of events above the S/N threshold due to thermal noise fluctuations, $N_A(I > 5\sigma)$ is the actual number of events detected above the S/N threshold, $\sqrt{N_E(I > 5\sigma)}$ and Δ_N are the uncertainties on the $N_E(I > 5\sigma)$, δE represents the uncertainties combined in quadrature, and p is the significance where for $p > 0.05$ indicates that events $> 5\sigma$ are consistent with thermal noise fluctuations. The significance p for the time averages at and above 5.12 ms were calculated via Monte Carlo simulations as described in Section 4.2.4. $N_E(I > 5\sigma)$ for the time averages at and above 5.12 ms were estimated by taking the mean of the probability distribution functions (PDF) in the histograms.
[a] GRB 111212A was observed over a period of 20 minutes.

pairs at lower DM steps (Figure 8). Here we perform an analytical calculation showing that the time series in each DM step at the lower end of the DM range can be treated as independent.

Our calculation assumes that a 5σ noise event is detected due to the addition of power sample fluctuations in the time/frequency plane. Based on this assumption, we consider the following scenarios: (1) the probability of two consecutive DM steps each having a 5σ event, since $\sim$50% of power samples are identical at the lower DM; and (2) the probability of two DM steps separated by one DM step each having a 5σ event, since $\sim$25% of power samples are identical at lower DM. In
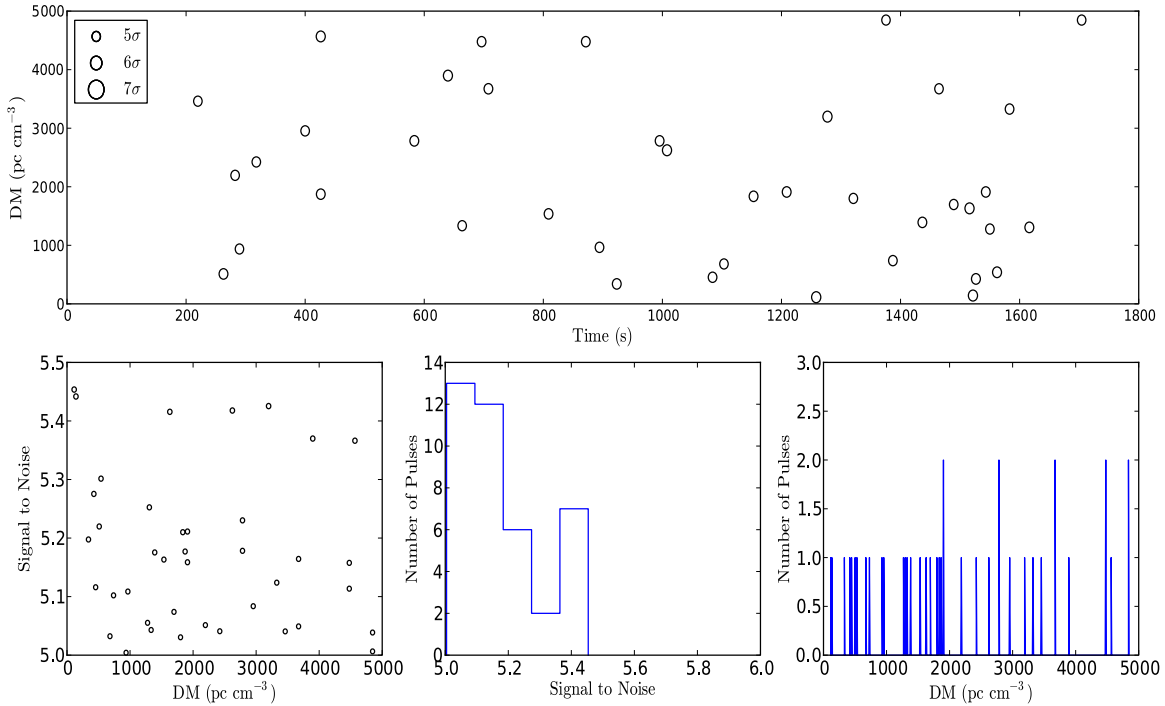
Figure 7. Example diagnostic plot that illustrates the distribution of detected events $>5\sigma$ for GRB 120211A at 1.28 ms time average. Top panel: all events with S/N $> 5\sigma$ plotted vs. DM and time. The size of circles are proportional to the S/N of the events. Lower left panel: scatter plot of the DM and S/N. Lower middle panel: distribution of the detected events $>5\sigma$. Lower right panel: number of detected events $>5\sigma$ vs. DM.

(A color version of this figure is available in the online journal.)
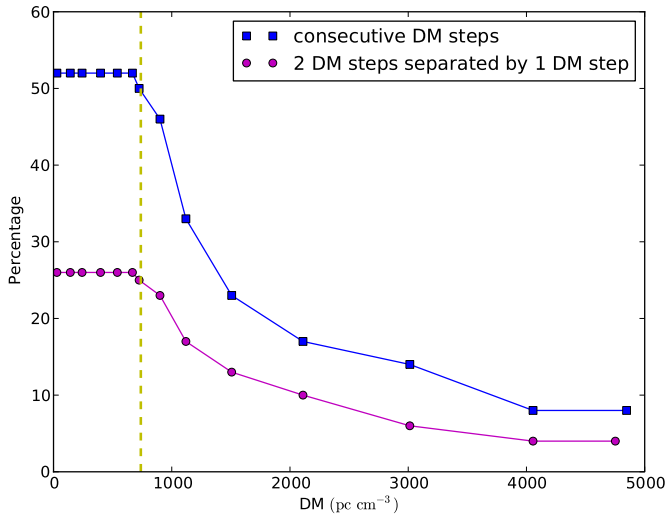
Figure 8. Percentage of identical power samples between consecutive DM steps at 640 μs time average. At lower DM (where DM steps are linearly distributed), $\sim$51%–52% of power samples are identical between the consecutive DM steps and $\sim$26%–27% of power samples are identical between the two DM steps separated by one DM step. However, at the higher DM (where DM steps are exponentially distributed), the number of identical power samples between DM steps reduces, which leads to less correlation in the dedispersed time series. The vertical dashed line represents the transition in the distribution of the DM steps from linear to exponential.

(A color version of this figure is available in the online journal.)

the former case, the probability is reduced by a factor of $\sim$100 compared with a single 5σ event in a DM step due to thermal noise fluctuations. In the latter case, the probability indicates that events $>5\sigma$ are consistent with events due to thermal noise fluctuations reduced by $\sim$10^6 (a detailed description of the calculation is given in the Appendix). The small probability in the former and latter scenarios implies that 5σ detections in

two or more DM steps at the lower end of the DM range are independent.

### 4.2.2. Uncertainties in the Estimation of $N_E(I > 5\sigma)$

The expected number of events due to thermal noise fluctuations, $N_E(I > 5\sigma)$, is uncertain due to two effects: (1) events detected due to thermal fluctuations are stochastic and their number is characterized by the Poisson distribution; (2) the variance measured from the data is a sample estimate, which has inherent uncertainty on the variance as it is being estimated over a finite number of samples. We take these effects into account in order to make our statistical analysis robust.

1. *Stochasticity of 5σ events*. We note that the thermal noise is stochastic in nature, inducing an uncertainty in the estimation of $N_E(I > 5\sigma)$ that can be quantified using the Poisson distribution. The probability of observing X events when λ number of events is expected is given by

$$\text{Pois}(X; \lambda) = \frac{\lambda^X \exp(-\lambda)}{X!}. \tag{3}$$

   For large λ, the Poisson distribution approximates the Gaussian distribution where $X \sim \text{Pois}(\lambda); \lambda \geqslant 15 \Rightarrow X \sim \mathcal{N}(\lambda, \lambda)$ (Hans-Joachim & Horst Rinne [1993]). Therefore, for $\lambda \geqslant 15$, we use the Gaussian approximation and the uncertainty in the number of events fluctuates around the mean ($\lambda = N_E(I > 5\sigma)$) with a standard deviation $\sqrt{N_E(I > 5\sigma)}$. For $N_E(I > 5\sigma) < 15$, the Gaussian approximation is invalid, and we use Monte Carlo (MC) simulations to estimate the uncertainties. This is described in Section 4.2.4.

2. *Sample variance in estimating true signal variance*. A finite number of samples ($N = 2048$ time samples at the intrinsic temporal resolution) are used to estimate the mean and the

(a) 5.12 ms　　　　　　　　　　　　　　　　(b) 10.24 ms
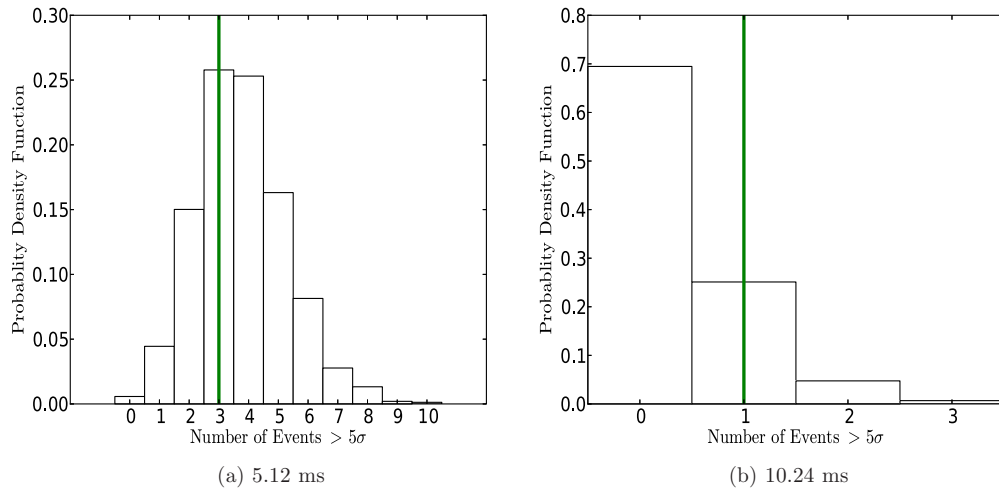
Figure 9. Left panel: example histogram obtained through MC simulations for GRB 120211A at 5.12 ms. The solid line in green represents the $N_A(I > 5\sigma)$ for GRB 120211A at 5.12 ms time average. Right panel: example histogram obtained through MC simulations for GRB 120211A at 10.24 ms. The solid line in green represents the $N_A(I > 5\sigma)$ for GRB 120211A at 10.24 ms time average.

(A color version of this figure is available in the online journal.)

standard deviation of the data. The true mean and standard deviation of the data are not known. This estimate has an associated uncertainty known as sample variance because only a finite number of samples are used. The standard error on the estimation of the mean ($\triangle \hat{I}_0$) and variance ($\triangle \hat{\sigma}^2$) for N independent samples from the true value are given by $\triangle \hat{I}_0 = (\sigma/\sqrt{N})$ and $\triangle \hat{\sigma}^2 = \sqrt{(2/(N-1))}\,\sigma^2$, respectively. The errors $\triangle \hat{I}_0$ and $\triangle \hat{\sigma}^2$ are propagated into the expression for the cumulative probability (Equation (2)) and the variance on the cumulative probability is obtained. For a detection threshold of 5σ, the variance is given by $(\Delta P)^2$,

$$(\Delta P)^2 = \frac{1}{2\pi} \exp(-5^2) \left(\frac{1}{N} + \frac{5^2}{N-1} \right), \qquad (4)$$

where N is the number of time samples. The sample size must be large enough to minimize the sample variance, but should not be so large that the mean changes with in the sample which would artificially increase the variance estimate.

The uncertainty in the expected number of events due to sample variance is propagated to an uncertainty in $N_E(I > 5\sigma)$ using Equations (1) and (4),

$$\Delta_N \equiv N_{\mathrm{DM}}\, N_t\, \Delta P. \qquad (5)$$

The two uncertainties in the estimate of $N_E(I > 5\sigma)$ are independent and Gaussian distributed, and therefore can be combined in quadrature,

$$\delta E^2 = (\sqrt{N_E(I > 5\sigma)})^2 \pm \Delta_N^2. \qquad (6)$$

4.2.3. Estimating the Significance of $N_A(I > 5\sigma)$ in Two Regimes

In the previous section, we combined the two uncertainties associated with the estimation of $N_E(I > 5\sigma)$ in quadrature, since both uncertainties obey Gaussian approximations. Here we would like to note again that the Gaussian approximation in case 1 is valid only for $N_E(I > 5\sigma) \gtrsim 15$. We observe from Tables 3 and 4 that for higher time averages ranging 5.12–25.5 ms, $N_E(I > 5\sigma) < 15$, the Gaussian approximation

for the uncertainty discussed in Section 4.2.2 is no longer valid. Therefore, for higher time averages (5.12–25.5 ms), we cannot combine both uncertainties in quadrature.

To estimate the significance p of the observed events ($N_A(I > 5\sigma)$), we split the calculations into two regimes: (1) at lower time averages ranging 640 μs–2.56 ms were $N_E(I > 5\sigma) \gtrsim 15$, we calculate p via the Gaussian approximation with mean $N_E(I > 5\sigma)$ and variance δE, given by Equations (1) and (6), respectively; (2) at higher time averages (5.12–25.5 ms) where $N_E(I > 5\sigma) < 15$, we use results obtained via MC simulation to estimate p. In both regimes, we interpret a $p > 0.05$ to be consistent with the null hypothesis that is that the observed events $N_A(I > 5\sigma)$ are consistent with noise.

In the low time average regime p is given by,

$$p = \frac{1}{2} - \frac{1}{2}\,\mathrm{erf}\left(\frac{N_A(I > 5\sigma) - N_E(I > 5\sigma)}{\sqrt{2}\,\delta E} \right). \qquad (7)$$

4.2.4. Estimating Significance p via Monte Carlo Simulations for Higher Time Averages

To determine the significance of the observed events ($N_A(I > 5\sigma)$) at higher time averages (when $N_E(I < 5\sigma) < 15$), we use the MC technique and perform 10^4 simulations of random data sets. The simulations were performed on the time averages in the range 5.12–25.60 ms. The results of the simulations automatically include the combined uncertainty due the thermal noise and sample variance.

Our program generates an array of Gaussian distributed random data sets of duration 30 minutes and n DM steps (where n is given in Table 2). The array is then passed through the event detection pipeline (described in detail in Section 3).

For each iteration, the MC simulation detects events $>5\sigma$. We performed 10^4 iteration for each time average. Figure 9 shows an example histogram for 5.12 and 10.28 ms time averages where we plot the events detected over 10^4 iterations. The values in each bin are normalized to plot the probability density function, such that the integral over the range is unity. The significance (p) is determined by integrating the values in the histogram greater than and equal to $N_A(I > 5\sigma)$ value for a given time average. For instance, from Table 3, the number of events, $N_A(I > 5\sigma)$, recorded for GRB120211A is three at 5.12 ms time resolution. The significance of $N_A(I > 5\sigma)$ at the 5.12 ms

Table 4
A Summary of the Statistical Analysis Performed on All the Blank Sky Data Sets

GRB Name	$N_E(I > 5\sigma)$	$N_A(I > 5\sigma)$	$\sqrt{N_E(I > 5\sigma)}$	Δ_N	δE	p
(a) 640 μs						
GRB 111212A[a]	15	15	4	12	12	0.52
GRB 120211A	83	83	8	49	49	0.50
GRB 120212A[b]	83	. . .	. . .	. . .	. . .	. . .
GRB 120218A	83	81	8	49	49	0.52
GRB 120224A	83	90	8	49	49	0.44
(b) 1.28 ms						
GRB 111212A[a]	8	1	3	9	9	0.77
GRB 120211A	32	28	6	36	36	0.54
GRB 120212A[b]	32	. . .	. . .	. . .	. . .	. . .
GRB 120218A	32	35	6	36	36	0.48
GRB 120224A	32	37	6	36	36	0.44
(c) 2.56 ms						
GRB 111212A[a]	3	1	1	4	4	0.68
GRB 120211A	11	9	3	18	18	0.54
GRB 120212A[b]	11	. . .	. . .	. . .	. . .	. . .
GRB 120218A	11	7	3	18	18	0.58
GRB 120224A	11	9	3	18	18	0.54
(d) 5.12 ms						
GRB 111212A[a]	0	0	. . .	. . .	. . .	1.00
GRB 120211A	3	5	. . .	. . .	. . .	0.14
GRB 120212A[b]	3	. . .	. . .	. . .	. . .	. . .
GRB 120218A	3	2	. . .	. . .	. . .	0.55
GRB 120224A	3	2	. . .	. . .	. . .	0.55
(e) 10.24 ms						
GRB 111212A[a]	0	0	. . .	. . .	. . .	1.00
GRB 120211A	0	0	. . .	. . .	. . .	1.00
GRB 120212A[b]	0	. . .	. . .	. . .	. . .	. . .
GRB 120218A	0	0	. . .	. . .	. . .	1.00
GRB 120224A	0	0	. . .	. . .	. . .	1.00
(e) 20.48 ms						
GRB 111212A[a]	0	0	. . .	. . .	. . .	1.00
GRB 120211A	0	0	. . .	. . .	. . .	1.00
GRB 120212A[b]	0	. . .	. . .	. . .	. . .	. . .
GRB 120218A	0	0	. . .	. . .	. . .	1.00
GRB 120224A	0	0	. . .	. . .	. . .	1.00
(e) 25.6 ms						
GRB 111212A[a]	0	0	. . .	. . .	. . .	1.00
GRB 120211A	0	0	. . .	. . .	. . .	1.00
GRB 120212A[b]	0	. . .	. . .	. . .	. . .	. . .
GRB 120218A	0	0	. . .	. . .	. . .	1.00
GRB 120224A	0	0	. . .	. . .	. . .	1.00

Notes. The subtables (a), (b), (c), (d), and (e) list the time averages used in this experiment. The columns are same as for Table 2.
[a] Blank sky was observed over a period of five minutes.
[b] No blank sky data were recorded due to insufficient storage space at the telescope.

time resolution can be calculated via the histogram summing the values greater than and equal to the bin number three (solid green line Figure 9(a)). The region in the histogram greater than and equal to $N_A(I > 5\sigma)$ value is termed the critical region[13] in statistics. Integrating the point probabilities greater than and equal to the critical value gives the significance p (Kay et al. 1998).

$N_E(I > 5\sigma)$ for each higher time average is given by the mean of the distribution, which is calculated by taking the average of values obtained through MC simulations (dotted lines in Figure 9). Here the duration of the random data sets was chosen to be the same as the observation duration for each GRB and blank sky data set.

4.2.5. Applying the Statistical Analysis on the Obtained Results

The statistical analysis was applied to all the GRBs for all averaging times. Table 3 presents the results of the analysis.

---

[13] Critical region in statistics is the portion of a statistics bloc where a null hypothesis is rejected via the results of a test of the hypothesis.

Table 5
Observational Parameters of This Work and B12

Parameters	12 m Parkes	26 m Hobart
Central frequency (MHz)	1340	2276
Bandwidth (MHz)	220	64
Time resolution (μs)	64	640
No. of channels	600	128
No. of polarizations	2	2
System equivalent flux density—SEFD (Jy)	3800	900
Min detectable flux density-1σ (Jy) @ 25 ms	1.07	0.5
Beam full width at half maximum (deg)	1.28	0.35
Average slew time (s)	175	140
S/N threshold	6	5

In all cases, $p > 0.05$, indicating that our recorded events are consistent with thermal noise fluctuations. In the absence of a characteristic signature of an astronomical pulse $>6\sigma$, we conclude that the events $>5\sigma$ are consistent with the expectations due to thermal noise fluctuations. There were no events with a statistically significant S/N.

Another approach to determine the probability of an event occurring due to thermal noise fluctuations is to measure the false positive rate when there is no GRB in the beam. Observing a patch of blank sky after the GRB observation preserves the noise properties and RFI information, assuming that no source of astronomical impulsive radio emission is in the field of view. We analyzed the data from the blank sky observations, which were processed in a manner identical to that described for the GRB data. Table 4 shows the results of our analysis for the blank sky data sets. Again, in all the cases $p > 0.05$ indicating that our recorded events are consistent with thermal noise fluctuations.

4.3. Discussion

In this section, we compare our results with the B12 and other previous experiment results to gain some understanding of the limits on FRB associated with GRBs and to give a quantitative assessment of the conclusions in B12.

4.3.1. Control Observation on Blank Sky

We have designed our experiment to be similar to B12 and have also made significant improvements. Firstly, unlike B12 we have undertaken control observations using blank patches of sky $\sim 2°$ away from the GRB positions. Secondly, the statistical analysis of the events detected from the blank sky gives estimates for the number of false positives due to thermal noise fluctuations and RFI. This method is more reliable when compared to the method adopted by B12 to account for the false positive rate by randomizing the spectral channels using data from the GRB observations. B12 showed that randomizing the spectral channels would preserve the properties of thermal noise fluctuations, narrow-band and wide-band RFI, but the presence of impulsive RFI that spans multiple channels are destroyed. This will reduce the number of false positive events due to thermal noise fluctuations and RFI. This effect will be high if the rate of impulsive RFI that spans over multiple channels is high, which leads to an inaccurate estimation of false positives. However, the data from blank sky taken $\sim 2°$ away from the GRB positions preserves all the properties of thermal noise fluctuations and RFI including the periodic and aperiodic RFI that spans multiple channels. Also, the data go through the same RFI excision and detection algorithms as those used for the GRB data sets, which should provide a more reliable estimate of the false positive rates.
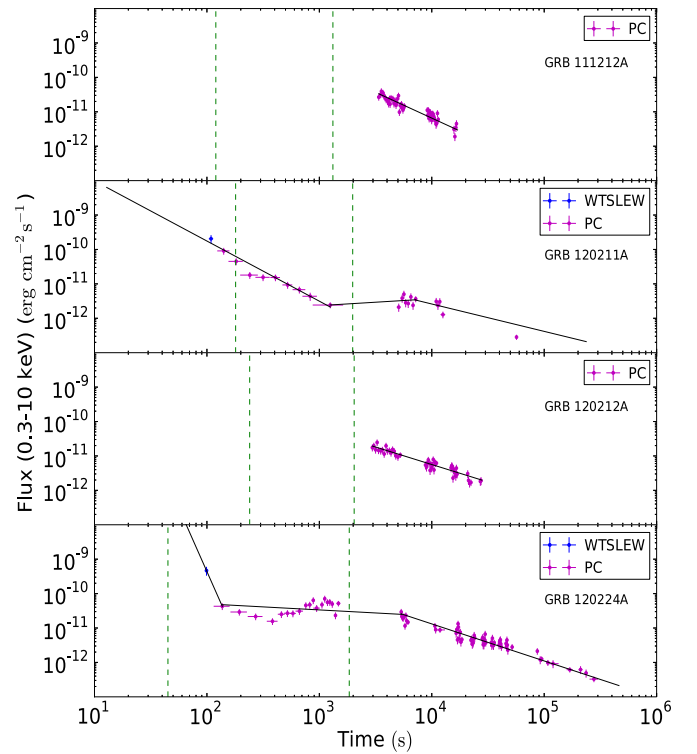
Figure 10. X-ray light curves for the four of the five GRBs observed in our experiment. The observation start (T_{on}) and end time are marked as vertical green lines. The black lines are the XRT powerlaw fits. WTSLEW/WT-settling is the window timing mode during the spacecraft slew. PC is the photon counting mode. For GRB 120218A, there is no XRT light curve due to Sun observing constraints. For GRB 111212A and GRB 120218A, no XRT prompt phase information was recorded due to *Swift* satellite orbital constrains. As the *Swift* satellite is in a low Earth orbit with the orbit period of 94 minutes, it suffers from 50% time off target per orbit.

(A color version of this figure is available in the online journal.)

4.3.2. Comparing the Experiment Parameters with B12

The average response times for our experiments and B12 are comparable. Table 5 compares the parameters of the B12 observations and our observations. We calculate that the 1σ flux density for our observations to detect a pulse width of 25 ms is approximately 0.5 Jy and for the B12 observations is 1.07 Jy, indicating that our observations are twice as sensitive as those by B12, (although at different frequencies). The two pulses detected by B12 are of >5 ms duration. Therefore, the difference in the minimum time resolution in both experiments is not likely to be significant.

4.3.3. The Similarity of the GRB X-Ray Light Curves

Figure 10 shows the X-ray light curves for the GRBs observed in our experiment and Figure 5 in B12 shows the X-ray light curves for the two GRBs for which radio pulses were detected by B12. The X-ray flux (F_ν, erg cm^{-2} s^{-1}) is given as $F_\nu \propto \nu^{-\beta_X} t^{-\alpha_X}$, where β_X is the spectral index, α_X is the temporal decay index, and t and ν are the time and frequency, respectively.

Evaluating Figure 10 and Figure 5 in B12, the X-ray telescope (XRT) typically starts observations $\sim 10^2$ s after the prompt γ-rays. The X-ray flux follows a typical pattern which comprises three distinct power-law segments as described by Nousek et al. (2006), Zhang et al. (2006), and O'Brien et al. (2006): (1) initial steep decay slope ($F_\nu \propto t^{-\alpha_X}$ with $3 \lesssim \alpha_{X,1} \lesssim 5$ and $t \sim 10^1$–10^2 s); (2) a very shallow decay ($0.5 \lesssim \alpha_{X,2} \lesssim 1.0$

Table 6
Temporal Indices ($\alpha_{X,1}$, $\alpha_{X,2}$, $\alpha_{X,3}$) of the X-ray Light Curves for the GRBs Observed in our Experiment and for
Two GRBs for which Radio Pulses were Detected B12

Source	$\alpha_{X,1}$	$t_{\text{break},1}$ (s)	$\alpha_{X,2}$	$t_{\text{break},2}$ (s)	$\alpha_{X,3}$	β_X^{d}
GRB 100704A[a]	3.09 ± 0.58	502	0.38 ± 0.30	1157	0.90 ± 0.08	1.12 ± 0.10
GRB 101011A[a]	2.54 ± 0.70	708	. . .	. . .	0.89 ± 0.17	0.81 ± 0.30
GRB 111212A[b]	. . .	. . .	. . .	. . .	1.49 ± 0.12	1.03 ± 0.14
GRB 120211A	1.74 ± 0.18	521	-0.19 ± 0.25	5082	0.79 ± 0.33	0.22 ± 0.21
GRB 120212A[b]	. . .	. . .	. . .	. . .	1.01 ± 0.07	1.08 ± 0.16
GRB 120218A[c]	. . .	. . .	. . .	. . .	. . .	. . .
GRB 120224A	7.38	136	0.01 ± 0.10	5348	1.07 ± 0.26	1.22 ± 0.14

Notes. $t_{\text{break},1}$ and $t_{\text{break},2}$ are the break times in second on the X-ray light curve. β_X is the spectral index in photon counting (PC) mode (Evans et al. 2009).
[a] Two GRBs from B12 experiment for which radio pulses were detected.
[b] No XRT prompt phase information was recorded due to *Swift* satellite orbital constrains. As the *Swift* satellite is in a low Earth orbit with the orbit period of 94 minutes, it suffers from 50% time off target per orbit.
[c] No X-ray light curve due to Sun observing constraints. *Swift* could not slew to the BAT position until 19:14 UT on 2012 February 20.
[d] The information on spectral index β_X were obtained from the *Swift* XRT archive.

and $t \sim 10^2$–10^3 s); and (3) a steep decay ($1.0 \lesssim \alpha_{X,3} \lesssim 1.5$ and $t \sim 10^3$–10^4 s). These segments are separated by two corresponding break times, $t_{\text{break},1} \lesssim 500$ s and $10^3 \lesssim t_{\text{break},2} \lesssim 10^4$ s.

Table 6 lists the temporal indices ($\alpha_{X,1}$, $\alpha_{X,2}$, $\alpha_{X,3}$) and spectral index (β_X) parameters for all the X-ray light curves in Figure 10 and Figure 5 in B12. The temporal indices and spectral indices for all the GRBs listed in Table 6 are consistent with the standard GRB X-ray light curve, indicating that the GRBs are from similar populations (although in many cases we do not see all three power-law segments, due to limited XRT coverage). Therefore, we note that the GRBs from which B12 claim FRB emission do not appear different from the GRBs we observed in our experiment.

4.3.4. Detection Statistics

Here we estimate the probability that the combined experiments detected FRB emission, over the combined observations reported in this experiment (hereafter P14) and in B12. Since many astrophysical objects follow a luminosity function with a power-law exponent (Macquart 2011), we assume GRBs are distributed homogeneously in a static Euclidean universe and each GRB generates an FRB with differential number density per unit flux given by

$$\frac{dN}{dS} \propto S^{-\alpha_r} = \mu S^{-\alpha_r}, \tag{8}$$

where $\alpha_r = 2.5$. In order to compare events at different frequencies, we assume the flux density of the FRB has a spectral index β_r over radio frequencies.

Based on these assumptions, we calculate the total probability of our experiment detecting zero events and B12 detecting two events out of eight. The total probability, P_{tot}, for both experiments is given by the joint probability distribution

$$P_{\text{tot}} = \prod_{i=1}^{2} P(S > S_{\text{min,B12}}) \times \prod_{i=1}^{6} P(S < S_{\text{min,B12}})$$
$$\times \prod_{i=1}^{5} P(S < S_{\text{min,P14}}), \tag{9}$$

where S is the flux density and $S_{\text{min,B12}}$ and $S_{\text{min,P14}}$ are the threshold flux densities for the B12 experiment and our experiment, respectively. $P(S > S_{\text{min,B12}})$ corresponds to the probability of detecting events, $> S_{\text{min,B}}$, and is given by

$$P(S > S_{\text{min,B12}}) = \frac{\int_{S_{\text{min,B12}}}^{\infty} \mu \, S^{-\alpha_r} \, dS}{\int_{S_0}^{\infty} \mu \, S^{-\alpha_r} \, dS} = \left(\frac{S_{\text{min,B12}}}{S_0}\right)^{-\alpha_r+1}, \tag{10}$$

where the denominator normalizes the distribution for a lower limit on the FRB flux density. We chose $S_0 = 0.189$ Jy to maximize P_{tot} for $\beta_r = 0$, hence to maximize the chance that the observed FRBs by B12 are astrophysical. The choice of S_0 corresponds to a low flux density cutoff in dN/dS that must exist for the probability of observing an FRB associated with any GRB to not be vanishingly small. Physically, this would correspond to a correlation between observed GRB flux density and FRB flux density. Testing the existence of such a correlation is an underlying motivation for this (and similar) experiments.

We note that the observing frequency and S/N threshold are different between our experiment and the B12 experiment (Table 5). The intrinsic spectral index is unknown. This difference is accounted for by scaling the flux density with a range of spectral indices $-5 \leqslant \beta_r \leqslant +5$, given by

$$S_{\text{min,B12}} = 6 \, \sigma_{\text{B12}} \left(\frac{\nu_{\text{P14}}}{\nu_{\text{B12}}}\right)^{\beta_r}, \tag{11}$$

where σ_{B12} is the minimum detectable flux density at 25 ms in B12 (Table 5), ν_{P14} and ν_{B12} are the central frequencies in our experiment and B12, respectively.

Next, we estimate P_{tot} in two regimes: (1) the probability of detecting zero events in our experiment and B12 detecting two events (from eight); and (2) the probability of detecting zero events in our experiment and B12 detecting one event (from eight). In the second case, we calculate the probability using Equation (10) just by changing the upper limit on first two terms of Equation (10). In the former case, the probability < 0.001 (top panel of Figure 11, solid red line) and in the latter case the probability $P_{\text{tot}} \lesssim 0.01$ (bottom panel of Figure 11, solid red line). This indicates that non-detections in our experiment are highly unlikely to be consistent with B12 having obtained two detections.

Table 7
Observation Parameters of Other GRB Experiments

Parameters	D96	S13[a]	O14[b]
Central frequency (MHz)	151	15270	74, 52, 37.9
Bandwidth	700 kHz	6 GHz	75 kHz
Time resolution (s)	1.5	0.5	5
Min detectable flux density-1σ (Jy) @ 25 ms	20	0.026	353, 336, 311
No. of GRBs observed	2	4	12, 5, 17
S/N threshold	3	3	5

Notes.
[a] The total number of GRBs observed by S13 was 11, out of which only four GRBs were observed within five minutes of the GRB notification. Hence we consider only four GRBs in the analysis.
[b] O14 observed 34 GRBs in total. However the sensitivity of the detector was different for each GRB. Here we have calculated the sensitivity by taking an average over the sensitivities at a given observing frequency.
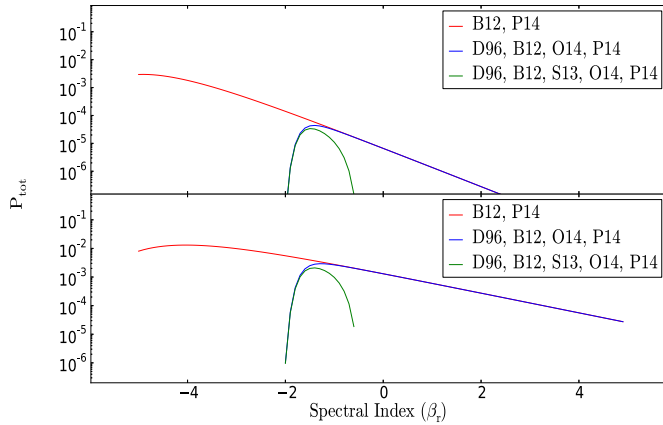
Figure 11. Top panel: the probability of detecting B12 detecting two events and zero events in other experiments as a function of β_r, spectral index. Bottom panel: the probability B12 detecting one real event and zero events in other experiments as a function of β_r, spectral index. S_0 is the low flux density cutoff. The three curves show the limit imposed by adding more experiments at different frequencies. The red solid line depicts the total probability for P14 and B12 experiments for the range of spectral indices. The blue solid line depicts the total probability of B12 finding events while the D96, O14, and P14 experiments have found no events. The green solid line depicts the total probability of finding events while the S13, D96, O14, and P14 experiments have found no events.

(A color version of this figure is available in the online journal.)

Next, we now extend the above analysis to include the experiments of Dessenne et al. (1996, hereafter D96), Staley et al. (2013, hereafter S13) and Obenberger et al. (2014, hereafter O14). Table 7 list the parameters for these experiments. The total probability of observed results over all five experiments is given by

$$
P_{\rm tot} = \prod_{i=1}^{2} P(S > S_{\rm min,B12}) \times \prod_{i=1}^{6} P(S < S_{\rm min,B12})
$$
$$
\times \prod_{i=1}^{5} P(S < S_{\rm min,P14}) \times \prod_{i=1}^{2} P(S < S_{\rm min,D96})
$$
$$
\times \prod_{i=1}^{34} P(S < S_{\rm min,O14}) \times \prod_{i=1}^{4} P(S < S_{\rm min,S13}). \quad (12)
$$

Similar to the above analysis, we calculate the total probability in two regimes: (1) the probability of detecting zero events in four different experiments and B12 detecting two events (from eight); and (2) the probability of detecting zero events in four different experiments and B12 detecting one event (from eight).

To illustrate the effects of adding the low-frequency experiments and the high-frequency experiments, we combine the experiments in two steps. First, low-frequency experiments by D96 and O14 are combined with the B12 and P14 experiments. Next, both high- and low-frequency experiments by S13, D96, and O14 are combined with the B12 and P14 experiments. The blue solid line in Figure 11 depicts the total probability of B12 finding events while the D96, O14, and P14 experiments have found no events. The green solid line in Figure 11 depicts the total probability of B12 finding events while the S13, D96, O14, and P14 experiments found no events. In both cases the probability of null detection in the S13, D96, O14, and P14 experiments, with B12 detecting at least one, is $<10^{-2}$.

The sensitivities of the S13, D96, and O14 experiments are scaled to detect a 25 ms pulse (Table 7). In Figure 11, we note a sharp cut-off in the curve because at this point the low-frequency and high-frequency experiments have $S_{\rm min}$ values less than S_0, which implies that the probability of detecting an event would be vanishingly small. Hence, the low-frequency experiments (D96 and O14) would have easily detected a 25 ms pulse with spectral index $\beta_r < -2$ given their detection thresholds, and the high-frequency experiment (S13) would have easily detected a 25 ms pulse with the spectral index $\beta_r > -0.5$.

Finally, we to note that including the other previous low-frequency experiments, Baird et al. (1975), Benz & Paesold (1998), and Balsano (1999), in the analysis makes no difference to the results.

5. CONCLUSION

This experiment searched for FRB-like emission from GRBs at 2.3 GHz. We observed five GRBs using a 26 m radio telescope, automated to quickly respond to GCN notifications and slew to the source position within minutes. We did not detect any sigma events $>6\sigma$ similar to B12, which motivated this experiment. Our analysis of events detected at $>5\sigma$ in our experiment shows that they are consistent with thermal noise fluctuations. Non-detections in our experiment agree with the lack of consistency between the event rates presented in Thornton et al. (2013) and GRB event rates.

A joint analysis of our results and four other GRB experiments shows that the B12 results are highly unlikely to be astrophysical. If B12 events are real, then the combined analysis constrains the radio spectral index of the events to be $-2 \lesssim \beta \lesssim -0.5$.
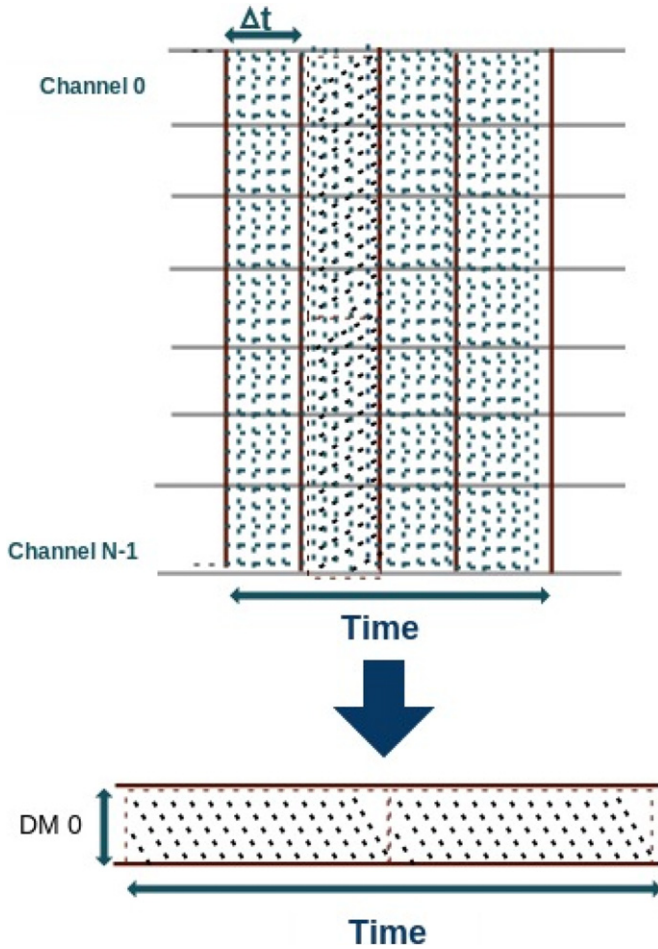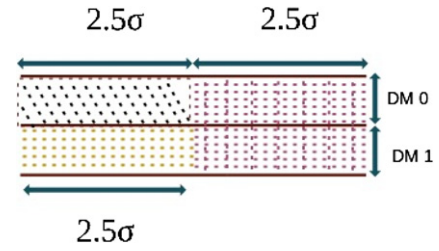
Figure 12. Top panel: data incoming into the dedisperser are ordered in frequency and time. The de-dispersion process sums the power samples across spectral channels, with the delay for each channel computed according to the frequency and DM. Bottom panel: for DM = 0, no delay is applied to the spectral channels and all the power samples are summed to form a time series.
(A color version of this figure is available in the online journal.)

Figure 13. Figure illustrates that ∼50% of power samples at DM of 1 overlaps with DM of 0 represented in dotted pink lines. And rest are the non-overlapping samples in the DM of 0 and 1 represented in dotted black and yellow lines.
(A color version of this figure is available in the online journal.)

power samples across spectral channels, with the delay for each channel computed according to the frequency and DM (Figure 12). Under normal circumstances, the power level in each spectral channel follows a Gaussian distribution.

For low DMs, there is a ∼50% overlap between the power samples that contribute to consecutive DM trials, at the same time. Here we demonstrate that this overlap does not correspond to a high level of correlation in detections between neighboring DM steps for a large (e.g., 5σ) detection threshold, and therefore that each DM step can be considered independent.

Let us consider a DM trial where the power samples in the channels are normally distributed across the spectrum. The variance of summing N_{chan} independent samples equals $N_{chan}\sigma_i^2$ and the standard deviation, $\sigma = \sqrt{N_{chan}}\,\sigma_i$, where σ_i is the noise level in a given power sample.

The probability of obtaining an event above a threshold, X, due to random addition of power sample fluctuations is given by the CDF:

$$P(I > X\sigma) = \frac{1}{2} - \frac{1}{2}\,\mathrm{erf}\left[\frac{X\sigma}{\sqrt{2}\,\sigma}\right]. \tag{A1}$$

Substituting $\sigma = \sqrt{N_{chan}}\,\sigma_i$ in Equation (A1), gives the CDF in terms of the noise level in each power sample:

$$P(I > X\sigma) = \frac{1}{2} - \frac{1}{2}\,\mathrm{erf}\left[\frac{X\sqrt{N_{chan}}\,\sigma_i}{\sqrt{2}\,\sqrt{N_{chan}}\,\sigma_i}\right]. \tag{A2}$$

The probability that we obtain a detection above our experimental threshold (5σ) from an independent DM step is given by

$$[P(I > 5\sigma)] = \frac{1}{2} - \frac{1}{2}\,\mathrm{erf}\left[\frac{5\sqrt{128}\,\sigma_i}{\sqrt{2}\,\sqrt{128}\,\sigma_i}\right] = 2.87 \times 10^{-7}, \tag{A3}$$

where $N_{chan} = 128$.

For low DMs, we note that due to our choice of progression in the DM steps, there is a ∼50% overlap between the power samples that contribute to consecutive DM trials at the same time. When there are shared samples between consecutive DM steps, those samples contribute the same power to both DM trials. There are many permutations for how power can be distributed in each set of power samples to combine to yield two detections above $X\sigma$. It can be shown that the power distribution with the highest joint probability over the two DM trials corresponds to the case shown in Figure 13, where the shared power samples contribute proportionally to the power required to meet the threshold. Under this scenario, *each* of the three sets of $N_{overlap} = 64$ samples contributes $2.5\sigma = 2.5\sqrt{N_{chan}}\sigma_i$.

APPENDIX

Data incoming into the dedisperser are discrete samples in frequency and time. The de-dispersion process sums the

The probability that each set obtains a detection $>2.5\sigma$ is given by

$$P_{\text{set}}(I > X_{\text{set}}\sigma) = \frac{1}{2} - \frac{1}{2} \text{erf}\left[\frac{X_{\text{set}}\sqrt{N_{\text{chan}}}\,\sigma}{\sqrt{2\,N_{\text{overlap}}}\,\sigma}\right], \qquad (A4)$$

with $X_{\text{set}} = X N_{\text{overlap}}/N_{\text{chan}} = 2.5$, giving

$$P(I > X\sigma) = \frac{1}{2} - \frac{1}{2}\text{erf}\left[\frac{X\sqrt{N_{\text{overlap}}}}{\sqrt{2\,N_{\text{chan}}}}\right]. \qquad (A5)$$

When 50% of samples overlap and the threshold, $X = 5$, the joint probability of obtaining detections in two consecutive DM trials is given by the product of the probability for each of the three sets

$$P(I > 5\sigma) = [P_{\text{set}}(I > 2.5\sigma\ ;\ N_{\text{overlap}} = 64)]^3 = 1.7 \times 10^{-9}. \qquad (A6)$$

This is $\sim$100 times smaller than the probability of detecting a single event (Equations (A1)–(A3)). Therefore, although the power samples contributing to the consecutive DM trials are 50% correlated due to the improbability of obtaining a single 5σ detection, the joint probability of obtaining two detections is very small. We therefore conclude that the DM trials can be considered statistically independent.

REFERENCES

Atwood, W. B., Abdo, A. A., Ackermann, M., et al. 2009, ApJ, 697, 1071
Baird, G. A., Delaney, T. J., Lawless, B. G., et al. 1975, ApJL, 196, L11
Balsano, R. J. 1999, PhD thesis, Princeton University
Bannister, K. W., & Madsen, G. J. 2014, arXiv:1402.0268
Bannister, K. W., Murphy, T., Gaensler, B. M., & Reynolds, J. E. 2012, ApJ, 757, 38
Benz, A. O., & Paesold, G. 1998, A&A, 329, 61
Burke-Spolaor, S., Bailes, M., Ekers, R., Macquart, J.-P., & Crawford, F., III. 2011, ApJ, 727, 18
Cordes, J. M., & Lazio, T. J. W. 2002, arXiv:astro-ph/0207156
Cordes, J. M., & McLaughlin, M. A. 2003, ApJ, 596, 1142
Crawford, F., Roberts, M. S. E., Hessels, J. W. T., et al. 2006, ApJ, 652, 1499
Dessenne, C. A.-C., Green, D. A., Warner, P. J., et al. 1996, MNRAS, 281, 977
Edwards, R. T., Bailes, M., van Straten, W., & Britton, M. C. 2001, MNRAS, 326, 358
Evans, P. A., Beardmore, A. P., Page, K. L., et al. 2009, MNRAS, 397, 1177

Fan, Y.-Z., Tam, P. H. T., Zhang, F.-W., et al. 2013a, ApJ, 776, 95
Fan, Y.-Z., Yu, Y.-W., Xu, D., et al. 2013b, ApJL, 779, L25
Fridman, P. A. 2008, AJ, 135, 1810
Gehrels, N., Chincarini, G., Giommi, P., et al. 2004, ApJ, 611, 1005
Gehrels, N., Ramirez-Ruiz, E., & Fox, D. B. 2009, ARA&A, 47, 567
Ghirlanda, G., Ghisellini, G., & Firmani, C. 2006, NJPh, 8, 123
Hans-Joachim, M., & Horst, R. 1993, Statistical Methods of Quality Assurance (Boca Raton, FL: CRC Press)
Ioka, K. 2003, ApJL, 598, L79
Jacoby, B. A., Bailes, M., Ord, S. M., Edwards, R. T., & Kulkarni, S. R. 2009, ApJ, 699, 2009
Kay, M. S. 1998, Fundamentals of Statistical Signal Processing Detection Theory (Englewood Cliffs, NJ: Prentice Hall PTR)
Keane, E. F., Kramer, M., Lyne, A. G., Stappers, B. W., & McLaughlin, M. A. 2011, MNRAS, 415, 3065
Kouveliotou, C., Meegan, C. A., Fishman, G. J., et al. 1993, ApJL, 413, L101
Lei, W.-H., Zhang, B., & Liang, E.-W. 2013, ApJ, 765, 125
Lorimer, D. R., Bailes, M., McLaughlin, M. A., Narkevic, D. J., & Crawford, F. 2007, Sci, 318, 777
Lorimer, D. R., & Kramer, M. 2012, Handbook of Pulsar Astronomy (Cambridge: Cambridge Univ. Press)
Macquart, J.-P. 2007, ApJL, 658, L1
Macquart, J.-P. 2011, ApJ, 734, 20
Manchester, R. N., Fan, G., Lyne, A. G., Kaspi, V. M., & Crawford, F. 2006, ApJ, 649, 235
Manchester, R. N., Hobbs, G. B., Teoh, A., & Hobbs, M. 2005, AJ, 129, 1993
Manchester, R. N., Lyne, A. G., Camilo, F., et al. 2001, MNRAS, 328, 17
Napier, P. J., Bagri, D. S., Clark, B. G., et al. 1994, IEEEP, 82, 658
Narayan, R., Piran, T., & Kumar, P. 2001, ApJ, 557, 949
Nousek, J. A., Kouveliotou, C., Grupe, D., et al. 2006, ApJ, 642, 389
Obenberger, K. S., Hartman, J. M., Taylor, G. B., et al. 2014, ApJ, 785, 27
O'Brien, P. T., Willingale, R., Osborne, J., et al. 2006, ApJ, 647, 1213
Palmer, D. M. 1993, ApJL, 417, L25
Phillips, C., Tzioumis, T., Tingay, S., et al. 2009, in 8th International e-VLBI Workshop (Trieste, Italy: SISSA)
Popham, R., Woosley, S. E., & Fryer, C. 1999, ApJ, 518, 356
Rees, M. J., & Meszaros, P. 1994, ApJL, 430, L93
Roberts, M. S. E., Hessels, J. W. T., Ransom, S. M., et al. 2002, ApJL, 577, L19
Rowlinson, A., O'Brien, P. T., Tanvir, N. R., et al. 2010, MNRAS, 409, 531
Spitler, L. G., Cordes, J. M., Hessels, J. W. T., et al. 2014, arXiv:1404.2934
Staley, T. D., Titterington, D. J., Fender, R. P., et al. 2013, MNRAS, 428, 3114
Tavani, M., Barbiellini, G., Argan, A., et al. 2009, A&A, 502, 995
Taylor, J. H. 1974, A&AS, 15, 367
Thornton, D., Stappers, B., Bailes, M., et al. 2013, arXiv:1307.1628
Usov, V. V. 1992, Natur, 357, 472
Usov, V. V., & Katz, J. I. 2000, A&A, 364, 655
Wayth, R. B., Brisken, W. F., Deller, A. T., et al. 2011, ApJ, 735, 97
Winkler, C., Courvoisier, T. J.-L., Di Cocco, G., et al. 2003, A&A, 411, L1
Zhang, B. 2014, ApJL, 780, L21
Zhang, B., Fan, Y. Z., Dyks, J., et al. 2006, ApJ, 642, 354